Novel Model for Rate Transient Analysis in Stress-Sensitive Shale Gas Reservoirs

Ting Lu,* Shengxiang Long, Zhiping Li, Shimin Liu, Yu Liu, Caspar Daniel Adenutsi, and Zeyang Peng
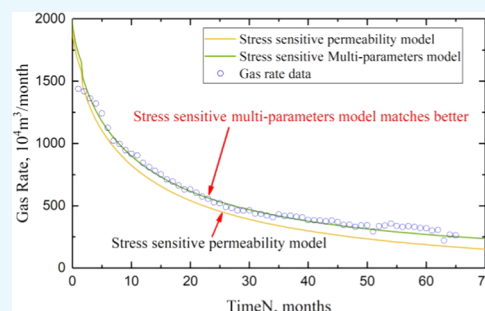
ACCESS | Metrics & More | Article Recommendations

ABSTRACT: Technical advances in hydraulic fracturing and horizontal drilling technologies enable shale to be commercially exploited. Due to the technical and economic limitations of well testing in shale gas plays, rate transient analysis has become a more attractive option. After hydraulic fracturing, flow mechanisms in multiple scaled pores of shale become extraordinarily complicated: adsorption in nanopores, diffusion in micropores, and non-Darcy flow in macropores. Moreover, shale gas reservoirs are stress-sensitive because of ultralow permeability and diffusivity in a matrix. Furthermore, the porosity and permeability of natural fractures are stress-dependent as well. Accounting for all of these complex flow mechanisms, especially the aforementioned stress-sensitive parameters, a semi-analytical production solution of a multiple fractured horizontal well (MFHW) can rapidly predict the entire production behavior. Scholars have done much work on the complex flow mechanisms of shale. Most models regarded permeability as a stress-sensitive parameter while diffusivity and porosity were considered to be a constant. However, diffusivity and porosity were proved to be stress-sensitive as experimental science developed. In this study, we present a novel semianalytical model for rate transient analysis of MFHW, which simultaneously incorporates multiple stress-sensitive parameters into flow mechanisms. Substituting stress-dependent parameters (diffusivity, porosity, and permeability) into governing equations resulted in strong nonlinearities, which was solved by employing the perturbation method. Production behaviors with only stress-sensitive permeability were compared with multiple stress-dependent parameters. The new model with multiple stress-sensitive parameters declined slower than the permeability-sensitive model, and the new model matched better with the field data. In addition, the effects of major stress-sensitive parameters on production decline curves were analyzed by the proposed model. The sensitivity analysis indicated that different parameters had their own degree of sensitivity intensity and influence on the production period. Finally, 1001 wells from the Marcellus shale play were divided into three well groups. Estimated inversion values of reservoir parameters from the three well groups and relevant single wells were consistent with the field data. The inverted values of single wells fluctuate within the inversion values of well groups, which indicates that the production behavior of well groups could be a guide for rate transient analysis of a single well in shale gas reservoirs.

1. INTRODUCTION

The advent of multistage fracturing and horizontal drilling technologies has had considerable success on shale gas development.[1] In addition, extensive hydraulic fracturing has increased shale gas production from fields.[2] There exist coherently multiple storage and flow mechanisms because of the small pore size and ultralow permeability of the shale matrix.[3−5] Characterization of shale is difficult because of the wide scale of pore sizes and types.[6] However, shale can be widely described as a dual-porosity medium according to the Warren−Root model[7] with: (1) micro-/mesopores within the shale matrix where gas transport is defined by the diffusive flow driven by a concentration gradient; (2) macropores in natural fractures where free gas is stored and its transport is dominated by a pressure gradient. As a dual-porosity reservoir, the pores within the matrix mainly serve as a storeroom where adsorption/desorption and diffusion occur, whereas the natural fractures provide the main gas pathways for mass transport with a Darcian flow.[8] Apart from the macropores, the shale formation also has hydraulic fractures, which provide main fluid-flow pathways during the entire production period. Thus, the flow of real gases through shale gas reservoirs is very complicated.[9] The overall gas deliverability of shale falls into a multimechanics flow regime including seepage flow, diffusion, and sorption.[10] Therefore, the gas production behavior characterization and prediction is expected to be a multimechanistic flow process.[11]
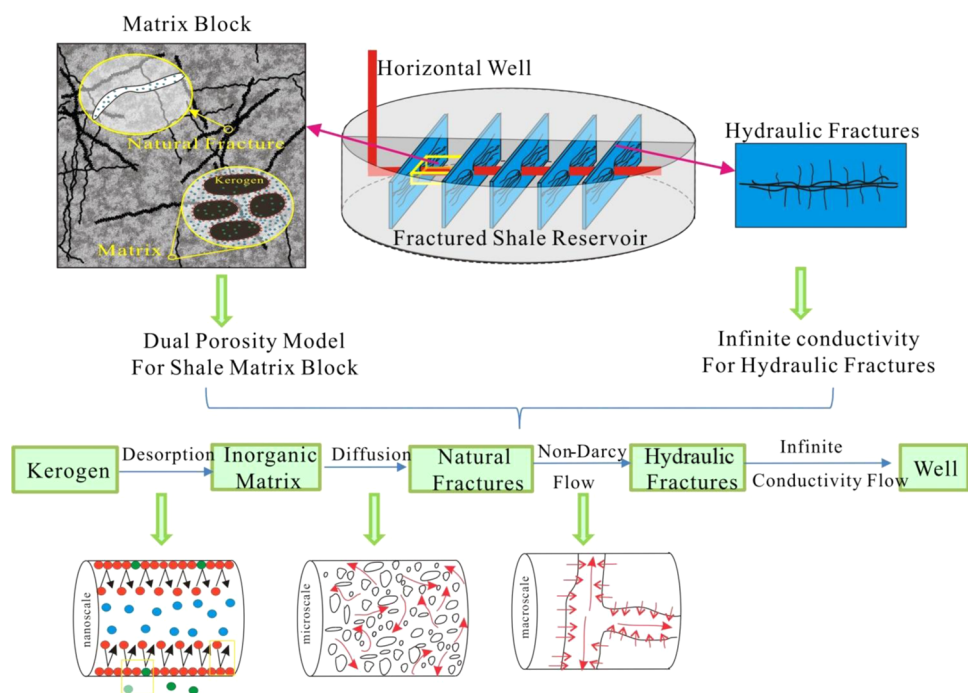
Figure 1. Conceptual model of a multiple fractured horizontal well (MFHW) in shale gas reservoirs.

Based on experimental data, the desorption phenomenon of shale gas can be described by the Langmuir isotherm theory.[12] Many other scholars also used the Langmuir isotherm theory to describe gas sorption in shale gas reservoirs.[13−15] Studies on the Langmuir isotherm theory involved many aspects. The Langmuir isotherm experiment can be conducted at high pressure and high temperature.[16] The Langmuir thermal adsorption theory can also be used to investigate sorption behaviors of multicomponent systems, such as methane and carbon dioxide sorption isotherms.[17] Recently, the relationship between organic matter and sorption has been extensively investigated. The effects of organic matter thermal maturity on methane sorption were quantified[18] and the Langmuir thermal adsorption theory was used to investigate how variations in the content and composition of the organic matter affect the growth of nanometer-scale pores.[19]

In shale, gas in the adsorbed layer is reported to be transported in the form of a diffusive flow by means of a concentration gradient.[20−22] By simultaneously considering Knudsen diffusion and slippage flow, a model was presented, which indicated that the effect of Knudsen diffusion is more pronounced and important within smaller pores.[10] Previous researchers showed that shale gas flow in nanopores can be modeled as a diffusive transport regime with a constant diffusion coefficient.[23] However, as exploitation and production of hydrocarbon continues, pore pressure decreases, which induces an increase in effective stress and this causes resistance to the fluid flow and reduces fluid storage.[24] In a recent study, the classical unipore pore model and the particle transport method were used to investigate the methane diffusion coefficient, and the results showed a negative correlation between the diffusion coefficient and pressure.[25,26] A nonlinear diffusion model was established by considering the diffusion of free gas in nanoscale pores as well as gas desorption on the surface of matrix particles.[27]

The permeability of tight/shale gas reservoir is extremely low and is highly related to pressure.[28−31] The permeability of shale gas reservoirs is proved to be stress-dependent by experimental work.[32,33] A numerical mathematical model was developed for gas flow incorporating the effect of stress-sensitive permeability.[34] Later, based on this model, the pressure transient behavior of the gas flow was simulated and it was pointed out that the test analysis results are not accurate unless stress dependence is taken into account.[35] Ostensen[36] concluded that stress sensitivity could reduce initial steady-state deliverability as much as 30% for inconsistent stress conditions. Apart from the aforementioned investigations, field practices also demonstrate the presence of stress sensitivity.[31] The influence of effective stress was studied on Barnett, Muskwa, Ohio, and Woodford shales and it was reported that the gas permeability increased as the effective stress decreased. The permeability of Marcellus shale is reported to be stress-dependent and had a negative correlation with confining pressure.[37] Furthermore, stress dependence affects rock porosity by changing the pore size.[38,39] Compared with permeability, stress dependence of porosity is small[24] but cannot be ignored when investigating stress-dependent diffusivity. Therefore, stress-dependent effects of porosity (matrix) and permeability (natural fractures) should be simultaneously taken into account during entire gas flow regimes.

Shale gas production involves multiscale pores and multi-mechanic flow regimes. Many scholars have been seeking appropriate methods to describe transient rate behaviors in stress-sensitive shale gas reservoirs. The influence of stress sensitivity on well production decline in constant wellbore pressure tests was analyzed, and variable property decline solutions did not follow the production decline type curves.[40] The empirical method mentioned above did not adequately consider flow mechanisms. A numerical model coupling geomechanical and fluid-flow aspects was established to discuss the effects of rock properties on productivity loss in stress-sensitive reservoirs.[41] A numerical simulator (dusty-gas model) with an adjusted Knudsen diffusion coefficient[42] was

used to characterize the flow regimes for tight and shale gas reservoirs, but desorption in the matrix and stress dependence of the fracture system were ignored. By incorporating gas adsorption, stress dependence, non-Darcy flow, and surface diffusion, an integrated model for shale gas reservoir simulation was proposed.[43−45] Apart from these models, shale gas numerical productivity models based on discrete fractures have also been established by many scholars.[46,47] The numerical method considered flow mechanisms and multiscale fractures but was quite time consuming. Semianalytical methods are also widely used. Production forecasts considering desorption are found to be more accurate.[48] A dual-mechanism dual-porosity linear model was established for gas transport in shale reservoirs by considering the diffusive flow in shale matrices and stress sensitivity of the fracture system.[49] However, desorption of shale gas was ignored in the proposed model. One of the shortcomings of linear models is that they cannot describe interference between hydraulic fractures. To overcome this, other researchers[50−54] established improved semianalytical models with a point source function. The stress sensitivity on the matrix and the fracture system found that either the matrix or the fracture subsystem has its passive influence on the transient production rate.[55] A semianalytical model was proposed for tight formation with a nonplanar fracture based on a volumetric source method.[56] These models incorporated multiple flow mechanisms (sorption, diffusion, and stress-sensitivity permeability) for shale gas reservoirs. The models are capable of matching some portions of gas production accurately. However, the late production behaviors could not be precisely predicted because diffusivity and porosity were assumed to be constant.

This work aims to establish a semianalytical rate transient analysis model for stress-sensitive shale gas reservoirs. Some improvements made into the new model include the addition of stress-dependent diffusivity and stress-dependent porosity, and averaging the well groups' production rate to represent a single well's performance. The proposed model is capable of estimating reservoir parameters when field data are available. It can also serve as a powerful tool for predicting gas production behaviors of the entire depletion stages. Moreover, inverted data set from the well group could be used as a guideline for interpreting a single well.

2. PHYSICAL MODEL AND ASSUMPTIONS

Horizontal well drilling and hydraulic fracturing are the most two crucial techniques for the commercial production of shale gas. After fracturing, the entire shale gas reservoir can be divided into two sections. One section is the hydraulic fractures, which are the main flow paths and assumed to have infinite conductivity in this study. The other section is the dual-porosity section containing natural and induced fractures and matrix blocks, which stores most of the free and adsorbed gas. Thus, the conceptual model, which contains a hydraulic fracture system and a matrix block system (matrix natural and induced fractures) is presented here. A full coupled multiscale flow model is presented for shale gas transport. Gas is stored as compressed free gas natural and induced fractures and as adsorbed gas within the shale matrices. As shown in Figure 1,[57] gas flows through a network of pores with different length scales ranging from nanometers to marcoscale pores.

Specifically, gas sorption happens on the internal surfaces of shale matrices within nanoscale pores. As the primary gas flux within the matrix, gas diffuses toward natural fractures by

Knudsen diffusion and slippage flow, which is dominated by a concentration gradient. Diffusivities within kerogen and an inorganic matrix are considered dynamic in this study because of the stress sensitivity in micropores and nanopores. As soon as the gas arrives at natural fractures, the gas flow obeys the seepage flow law dominated by a pressure gradient. The permeability and porosity of the natural fracture system are also stress-sensitive since the fracture closes as pressure drops.

From the physical standpoint, an idealized naturally fractured reservoir is considered to be a dual-porosity isotropic reservoir, which consists of a matrix and a natural fracture system. Gas flows radially and converges toward the multiple fractured horizontal well (MFHW), which is centrally located in a circular reservoir with sealed outer boundaries. Moreover, some assumptions must be made to satisfy the formulation of the mathematical model and these include: (1) diffusivity in the matrix is stress-sensitive and cannot be assumed to be constant. (2) Permeability and porosity of natural fractures are stress-dependent as natural fractures close with pressure depletion. (3) Hydraulic fractures have infinite conductivity as their permeability is much higher than natural fracture systems. (4) The MFHW produces at a constant rate in a finite reservoir. (5) The initial pressure throughout the reservoir is uniform and equal to p_i. (6) Gravity and capillary forces are negligible. (7) The boundaries are cylindrical and are all sealed. In the following sections, this conceptual model is formulated into a set of governing equations, which are subsequently implemented in a commercial programming software (MAT-LAB), and the results are discussed.

3. METHODS OF ANALYSIS AND THE WORKFLOW

As discussed in the previous subsection, the entire fractured shale gas reservoir has been divided into three parts, namely,
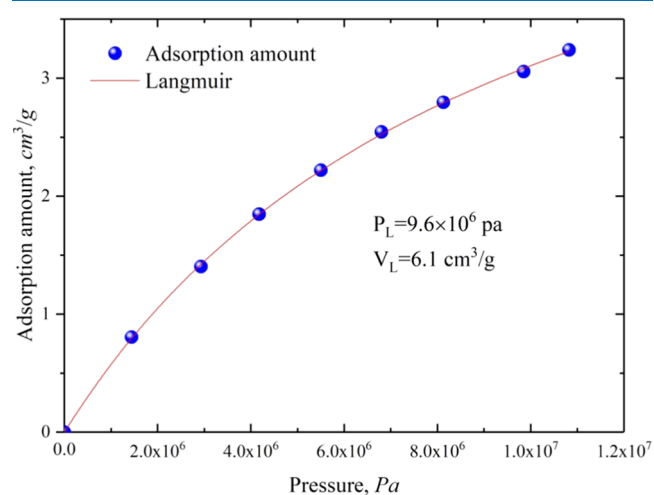
Figure 2. CH_4 isotherm sorption in the Marcellus shale by the Langmuir model.

matrix, natural fractures, and hydraulic fractures. As the hydraulic fractures are assumed to have infinite conductivity and there is no resistance to gas flow, the pressure in the hydraulic fractures is approximately equal to the pressure in the natural fracture next by. To this end, the gas flow in the matrix and natural fracture systems is thoroughly discussed.

3.1. Mathematical Model. *3.1.1. Governing Equations of the Matrix Block.* The sample used in this experiment was from the outcrop of Marcellus shale. The experiment was
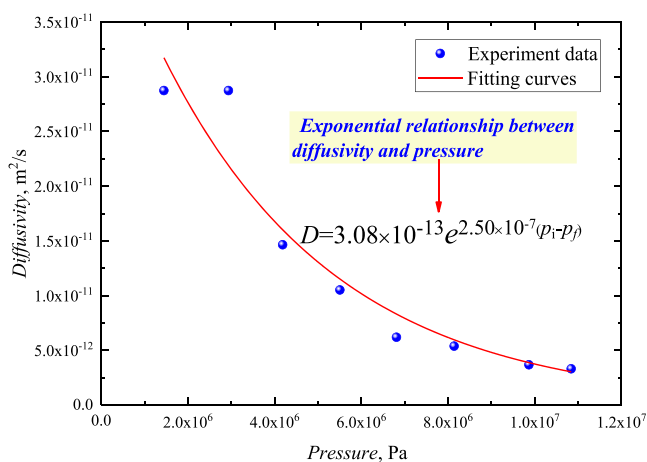
Figure 3. Diffusivity versus pressure in the Marcellus shale.

Table 1. Definitions of Dimensionless Variables

variables	expressions
dimensionless pseudopressure	$\psi_D = \dfrac{\pi k_{fi} h T_{sc}}{p_{sc} q_{sc} T} \Delta\psi, \; \Delta\psi = \psi_i - \psi$
dimensionless radius	$r_D = \dfrac{r}{L_{ref}}$
dimensionless equivalent controlling radius	$r_{eD} = \dfrac{r_e}{L_{ref}}$
dimensionless time	$t_D = \dfrac{k_{fi} t}{\mu_{gi} L_{ref}^2 \left[\phi C_{gi} + \dfrac{2\pi k_{fi} h}{q_{sc}\mu_{gi}}(1-\phi)\right]}$
dimensionless radius of the matrix	$r_{mD} = \dfrac{r_m}{R_m}$
dimensionless permeability modulus	$\gamma_D = \dfrac{\mu Z \gamma p_{sc} q_{sc} T}{2 p_f \pi k_{fi} h T_{sc}}$
dimensionless diffusivity modulus	$\delta_D = \dfrac{\mu Z \delta p_{sc} q_{sc} T}{2 p_f \pi k_{fi} h T_{sc}}$
dimensionless production rate of line source	$\tilde{q}_{fD} = \dfrac{\tilde{q}_f}{q_{sc}}$
dimensionless flux per unit length of the discrete segment (i, j)	$q_{Dij} = \dfrac{q_{ij} L_{ref}}{q_{sc}}$
dimensionless production	$q_D = \dfrac{q_{sc} p_{sc}}{\pi k_{fi} h T_{sc}(\psi_{fi} - \psi_{wf})}$
dimensionless length of the discrete segment (i, j)	$\Delta L_{fDij} = \dfrac{\Delta L_{fij}}{L_{ref}}$
storativity ratio	$\omega = \dfrac{\phi C_{gi}}{\phi C_{gi} + \dfrac{2\pi k_{fi} h}{q_{sc}\mu_{gi}}(1-\phi)}$
interporosity coefficient	$\lambda = \dfrac{\mu_{gi} L_{ref}^2 D_i \left[\phi C_{gi} + \dfrac{2\pi k_{fi} h}{q_{sc}\mu_{gi}}(1-\phi)\right]}{k_i R_m^2}$
adsorption index	$\sigma = \dfrac{p_{sc} q_{sc} T}{\pi k h T_{sc}} \dfrac{\psi_L V_L}{(\psi_L + \psi_i)^2}$

conducted at room temperature and at a pressure range of $(1-12) \times 10^6$ Pa. The sorption data with the Langmuir theory are shown in Figure 2. Combined with a single-pore model, the

Table 2. Values of Basic Parameters for the Synthetic Model

parameters	unit	value
formation thickness, h	m	31.11
porosity, ϕ	decimal	0.05
initial pressure, p_i	Pa	3.77×10^7
rock compressibility, C_f	Pa^{-1}	1.5×10^{-10}
gas compressibility, C_g	Pa^{-1}	4×10^{-8}
initial absolute permeability of fracture, k_{fi}	m^2	1×10^{-17}
permeability of matrix, k_m	m^2	1×10^{-24}
reservoir temperature, T	K	355.84
Langmuir volume, V_L	m^3/m^3	15.21
Langmuir pressure, p_L	Pa	1.2×10^7
number of fractures, M	dimensionless	15
the horizontal length of the MFHW, L	m	1374
fracture spacing, D_f	m	60
Wellbore diameter, r_w	m	0.108
gas initial viscosity, μ_{gi}	Pa·s	2×10^{-5}
gas initial compressibility factor, Z_i	m^3/m^3	0.97
Knudsen diffusivity, D_k	m^2/s	1×10^{-12}
matrix equivalent pore radius, R_m	m	1×10^{-8}
constant production, q_{sc}	m^3/s	1.04
reference length, L_{ref}	m	0.1

relationship between diffusivity and pressure is shown in Figure 3.

The Langmuir isotherm sorption theory is mostly used to describe the relationship between adsorption amount and pressure, which can be expressed as eq 1.[58] Fitting with experiment data by the Langmuir isotherm sorption equation, the Langmuir pressure and Langmuir volume are equal to 9.6 × 10^6 Pa and 6.1 cm^3/g, respectively,

$$V = V_L \frac{p}{p_L + p} \qquad (1)$$

where p_L is the Langmuir pressure, which is equal to 9.6 × 10^6 Pa in this experiment and V_L is the Langmuir volume and equal to 6.1 cm^3/g.

When the density distribution of gas in the shale is nonuniform, natural gas moves from a region of high density to a region of low density. This reduces the fluid density in the original high-density region but increases the fluid density in the low-density region. This phenomenon is called diffusion. For a dual-porosity medium, the flow pattern can be classified and characterized. From coalbed methane research, the pores of shale matrix systems are assumed to be spherical or the matrix is regarded as a spherical matrix.[59] The diffusion is assumed to follow the unipore model[60] and the infinite series solution of diffusion is described as follows

$$\frac{M_t}{M_\infty} = 1 - \frac{6}{\pi^2} \sum_{n=1}^{\infty} \frac{1}{n^2} \exp\left(\frac{-D_F n^2 \pi^2}{a_p^2} t\right) \qquad (2)$$

The model for the methane diffusion coefficient in coal[25] is introduced here to calculate the diffusion coefficient with isotherm sorption data. Based on the experiment data of the Langmuir isotherm sorption and eq 2, the diffusivity is stress-sensitive, which is consistent with a previous study.[27] In addition, there is an exponential correction between diffusivity and pressure, as shown in Figure 3. The relationship between diffusivity and pressure can be expressed as follows

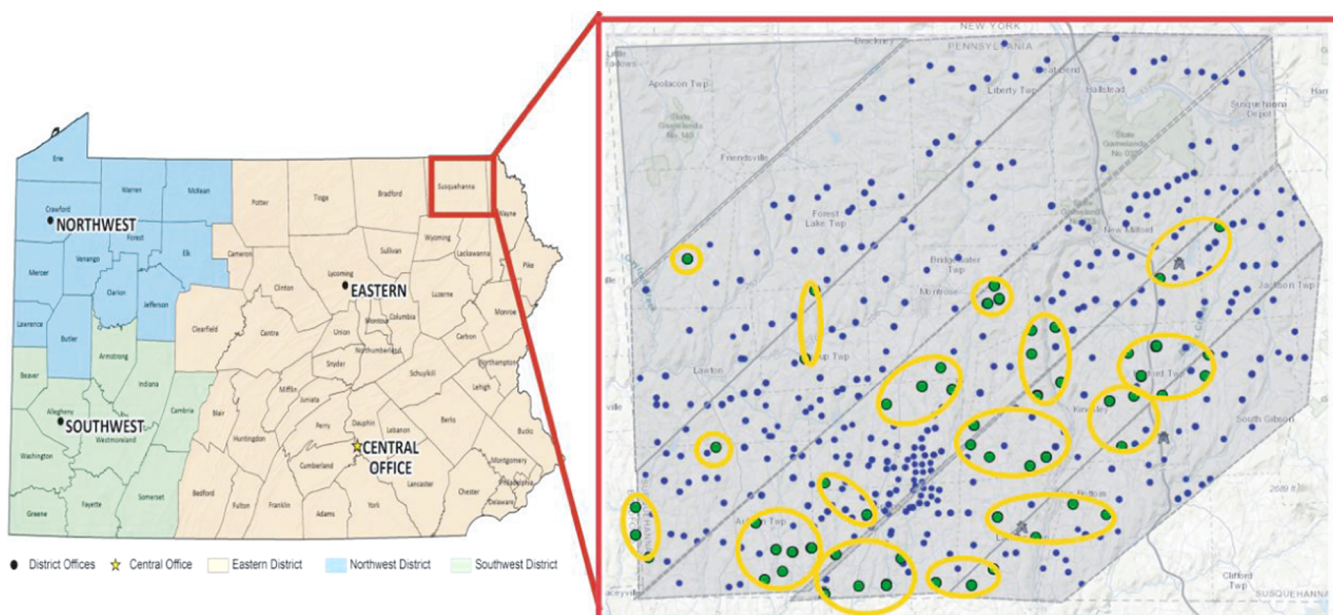$$D = D_i \, e^{\delta(p_i - p_f)} \qquad (3)$$

Figure 4. Map of Susquehanna County and its producing wells (high productive wells in yellow circles).
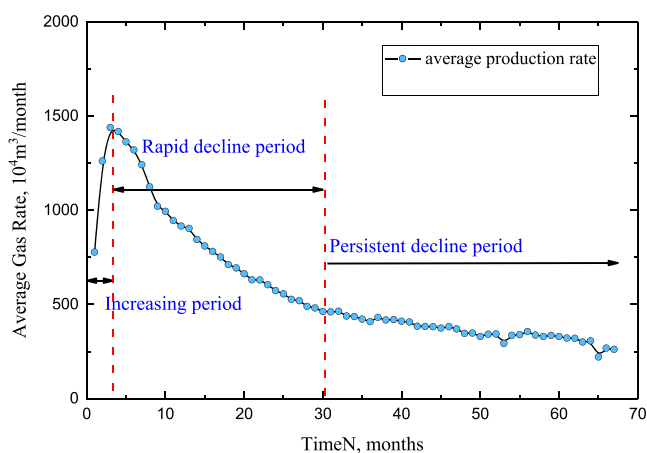
Figure 5. Average production rate of the high productive well group.
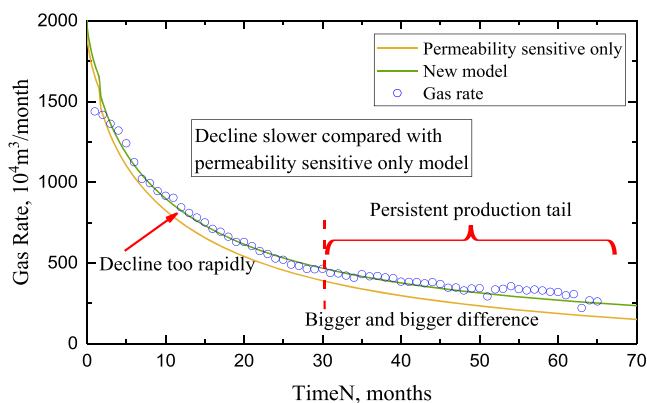
Figure 6. Comparison between field data and modeling results in the Marcellus Shale.

Table 3. Basic Values of Sensitive Parameters for the Synthetic Model

variables	units	values
initial permeability of natural fractures, k_{fi}	m^2	1.1×10^{-16}
initial porosity of natural fractures, ϕ_i	dimensionless	0.001
dimensionless sensitive modulus, $\gamma_D + \delta_D$	dimensionless	0.01
horizontal length, L	m	2000
fracture number, M	integer	20
fracture spacing, d_f	m	150
controlling radius, r_e	m	635
effective height, h	m	80
initial diffusivity, D_i	m^2/s	3×10^{-11}
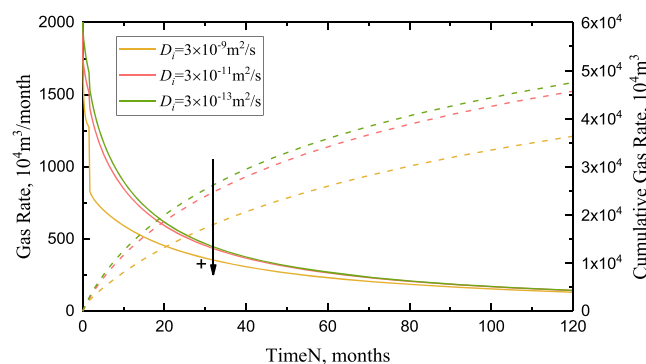
Figure 7. Effect of initial diffusivity on the production rate and cumulative production.

The partial differential equation of transient diffusion in a shale matrix obeys Fick's second law[61]

$$\frac{1}{r_m^2} \frac{\partial}{\partial r_m} \left[r_m^2 D \frac{\partial V}{\partial r_m} \right] = \frac{\partial V}{\partial t}$$

(4)

where r_m is the matrix pore radius, m; V is the volumetric gas concentration, m^3/m^3; and D is the diffusion coefficient, m^2/s.

As matrix blocks are assumed to be spherical, the transient diffusive flow is expressed as follows[62]

where D_i is the initial diffusion coefficient, m^2/s; δ is the diffusivity modulus, dimensionless; p_i is the initial pressure, Pa; and p_f is the pressure of the natural fracture system, Pa.
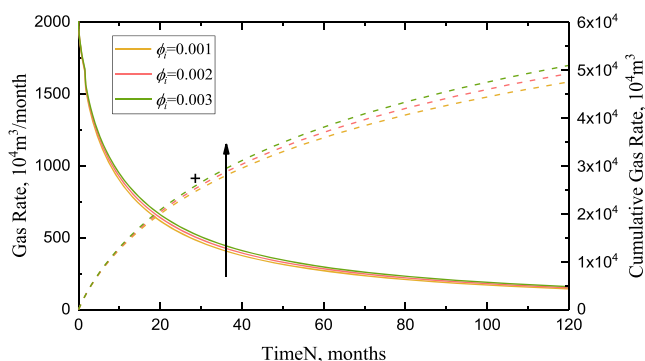
Figure 8. Effect of initial porosity of natural fractures on the production rate and cumulative production.
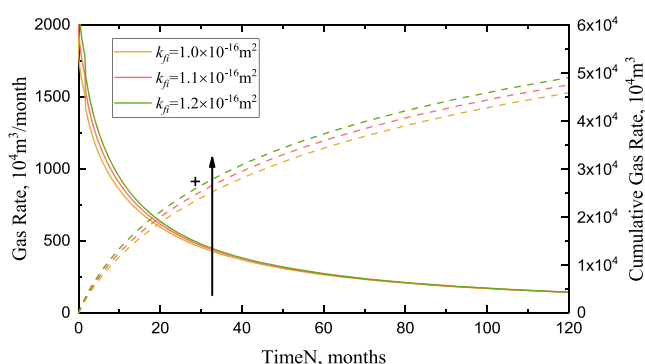
Figure 9. Effect of initial permeability of natural fractures on the production rate and cumulative production.
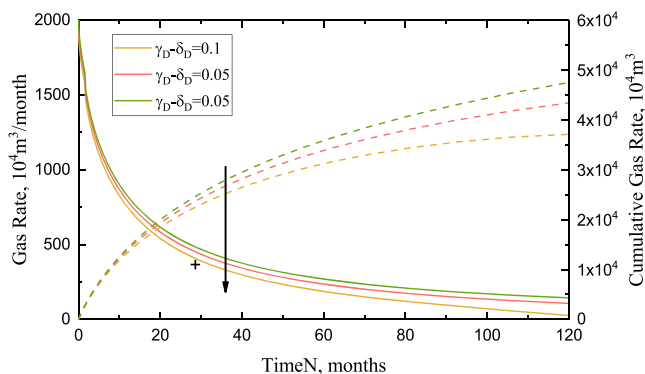
Figure 10. Effect of dimensionless sensitive modulus on the production rate and cumulative production.

$$\frac{\partial V}{\partial t} = \frac{3D}{R_{\mathrm{m}}} \frac{\partial V}{\partial r_{\mathrm{m}}}\bigg|_{r_{\mathrm{m}}=R_{\mathrm{m}}} \tag{5}$$

where R_{m} is the equivalent matrix pore radius, m.

The initial condition is expressed as

$$V|_{t=0} = V_{\mathrm{i}} \tag{6}$$

The center of the matrix is treated as a no-flow boundary as diffusion in the spherical matrix is symmetric. Thus, the inner boundary condition is expressed as

$$\frac{\partial V}{\partial r_{\mathrm{m}}}\bigg|_{r_{\mathrm{m}} \to 0} = 0 \tag{7}$$

The gas concentration on the surface of the bulk matrix is approximately equal to that in the natural fracture system. The outer boundary condition is therefore presented as

$$V|_{r_{\mathrm{m}}=R_{\mathrm{m}}} = V_{\mathrm{E}} \tag{8}$$

Note: L_{ref} is the arbitrary length and is assumed to be equal to r_{w}.

With the definitions of dimensionless variables in Table 1, eqs 4–8 can be rewritten as follows

$$\frac{1}{r_{\mathrm{mD}}^2} \frac{\partial}{\partial r_{\mathrm{mD}}} \left(r_{\mathrm{mD}}^2 \frac{\partial V_{\mathrm{D}}}{\partial r_{\mathrm{mD}}} \right) = \frac{1}{\lambda \ \mathrm{e}^{-\delta(p_{\mathrm{i}}-p_{\mathrm{f}})}} \frac{\partial V_{\mathrm{D}}}{\partial t_{\mathrm{D}}} \tag{9}$$

$$\frac{\partial V_{\mathrm{D}}}{\partial t_{\mathrm{D}}} = 3\lambda \ \mathrm{e}^{-\delta(p_{\mathrm{i}}-p_{\mathrm{f}})} \frac{\partial V_{\mathrm{D}}}{\partial r_{\mathrm{mD}}}\bigg|_{r_{\mathrm{mD}}=1} \tag{10}$$

$$\frac{\partial V_{\mathrm{D}}}{\partial r_{\mathrm{mD}}}\bigg|_{r_{\mathrm{mD}} \to 0} = 0 \tag{11}$$

$$V_{\mathrm{D}}|_{r_{\mathrm{mD}}=1} = V_{\mathrm{ED}} \tag{12}$$

$$V_{\mathrm{D}}|_{t_{\mathrm{D}}=0} = 0 \tag{13}$$

The derivation procedure of eqs 9–13 is shown in Appendix and the solution is as follows

$$s\overline{V_{\mathrm{D}}} = 3\lambda \ \mathrm{e}^{-\delta(p_{\mathrm{i}}-p_{\mathrm{f}})} \frac{\mathrm{d}V_{\mathrm{D}}}{\mathrm{d}r_{\mathrm{mD}}}\bigg|_{r_{\mathrm{mD}}=1}$$
$$= 3\sigma\lambda \ \mathrm{e}^{-\delta(p_{\mathrm{i}}-p_{\mathrm{f}})} [\sqrt{s/\lambda} \ \coth(s/\lambda) - 1]\overline{\psi_{\mathrm{fD}}} \tag{14}$$

3.1.2. Governing Equations of the Natural Fracture System. The diffusivity equation that describes the multi-mechanism flow in the natural fracture system for a shale gas reservoir is given by

$$\frac{1}{r} \frac{\partial}{\partial r}\left(r k_{\mathrm{f}} \frac{p_{\mathrm{f}}}{\mu_{\mathrm{g}} Z} \frac{\partial p_{\mathrm{f}}}{\partial r} \right) = \phi_{\mathrm{f}} \mu_{\mathrm{g}} C_{\mathrm{g}} \frac{p_{\mathrm{f}}}{\mu_{\mathrm{g}} Z} \frac{\partial p_{\mathrm{f}}}{\partial t} + \frac{p_{\mathrm{sc}} T}{T_{\mathrm{sc}}} \frac{\partial V}{\partial t} \tag{15}$$

where μ_{g} is gas viscosity at the current pressure, Pa·s and C_{g} is gas compressibility in the matrix, Pa^{-1}.

The permeability modulus that measures the dependence of hydraulic permeability on pore pressure is defined as[38]

$$k_{\mathrm{f}} = k_{\mathrm{fi}} \ \mathrm{e}^{-\gamma(p_{\mathrm{i}}-p_{\mathrm{f}})} \tag{16}$$

The porosity of the fracture system is also dependent on pore pressure.[38,63] The expression is as follows

$$\phi_{\mathrm{f}} = \phi_{\mathrm{fi}} \ \mathrm{e}^{-\delta(p_{\mathrm{i}}-p_{\mathrm{f}})} \tag{17}$$

As adapted from ref[64,65], the default value of γ is equal to 1.5 × 10^{-7}. Substituting eqs 16 and 17 into eq 15 yields the governing equation, which describes shale gas flow in a permeability and porosity stress-sensitive reservoir.

$$\frac{1}{r} \frac{\partial}{\partial r}\left(r k_{\mathrm{fi}} \ \mathrm{e}^{-\gamma(p_{\mathrm{i}}-p_{\mathrm{f}})} \frac{p_{\mathrm{f}}}{\mu_{\mathrm{g}} Z} \frac{\partial p_{\mathrm{f}}}{\partial r} \right)$$
$$= \phi_{\mathrm{fi}} \ \mathrm{e}^{-\delta(p_{\mathrm{i}}-p_{\mathrm{f}})} \mu_{\mathrm{g}} C_{\mathrm{g}} \frac{p_{\mathrm{f}}}{\mu_{\mathrm{g}} Z} \frac{\partial p_{\mathrm{f}}}{\partial t} + \frac{p_{\mathrm{sc}} T}{T_{\mathrm{sc}}} \frac{\partial V}{\partial t} \tag{18}$$

The definition of pseudopressure is given as

$$\psi = \int_{P_0}^{p} \frac{2p}{\mu_g Z} dp \tag{19}$$

The natural gas viscosity μ_g and natural gas compressibility C_g in eq 18 are pressure-dependent parameters. For simple calculation, μ_g and C_g can be approximately equal to the parameters under the initial pressure, that is, $\mu_g = \mu_{gi}$ and $C_g = C_{gi}$. Thus, the governing equation of the natural fracture system is

$$\frac{\partial^2 \psi_f}{\partial r^2} + \frac{1}{r}\frac{\partial \psi_f}{\partial r} + \frac{\mu_g Z}{2p}\gamma\left(\frac{\partial \psi_f}{\partial r}\right)^2$$
$$= e^{\mu_{gi}Z/2p(\gamma-\delta)(\psi_i-\psi_f)}\left[\frac{\phi_{fi}\mu_{gi}C_{gi}\partial\psi_f}{k_{fi}\partial t} + \frac{2p_{sc}T\partial V}{k_{fi}T_{sc}\partial t}\right] \tag{20}$$

3.1.3. Coupling Model for the Matrix Block and the Natural Fracture System.
From eqs 14 and 20, the coupling model in a dimensionless form for a matrix block and a natural fracture system is shown as

$$\frac{\partial^2 \psi_{fD}}{\partial r_D^2} + \frac{1}{r_D}\frac{\partial \psi_{fD}}{\partial r_D} + \gamma_D\left(\frac{\partial \psi_{fD}}{\partial r_D}\right)^2$$
$$= e^{(\gamma_D-\delta_D)\psi_{fD}}\left[\omega\frac{\partial \psi_{fD}}{\partial t_D} + (1-\omega)\frac{\partial V_D}{\partial t_D}\right] \tag{21}$$

Adding stress-sensitive parameters results in strong non-linearity in the partial differential equation. This can be solved by Pedrosa's substitution function.[66]

$$\psi_{fD}(r_D, t_D) = -\frac{1}{\gamma_D - \delta_D}\ln[1 - (\gamma_D + \delta_D)\xi_D(r_D, t_D)] \tag{22}$$

Substituting eq 22 into eq 21 yields

$$\frac{\partial^2 \xi_D}{\partial r_D^2} + \frac{1}{r_D}\frac{\partial \xi_D}{\partial r_D} = \frac{1}{1 - (\gamma_D - \delta_D)\xi_D}$$
$$\left[\omega\frac{\partial \xi_D}{\partial t_D} + (1-\omega)\frac{\partial V_D}{\partial t_D}\right] \tag{23}$$

Compared to eq 21, the nonlinearity of eq 23 considerably reduced due to Pedrosa's substitution. In addition, a perturbation technique is employed to derive an approximate analytical solution by performing a parameter perturbation in γ_D. This is defined as the following series

$$\xi_D = \xi_{D0} + \gamma_D\xi_{D1} + \gamma_D^2\xi_{D2} + \cdots \tag{24}$$

$$-\frac{1}{\gamma_D - \delta_D}\ln[1 - (\gamma_D - \delta_D)\xi_D(r_D, t_D)]$$
$$= \xi_D(r_D, t_D) + \frac{1}{2}\xi_D^2(r_D, t_D) + \cdots \tag{25}$$

$$\frac{1}{1 - (\gamma_D - \delta_D)\xi_D(r_D, t_D)}$$
$$= 1 + (\gamma_D - \delta_D)\xi_D(r_D, t_D) + (\gamma_D + \delta_D)^2\xi_D(r_D, t_D)$$
$$+ \cdots \tag{26}$$

The zero-order perturbation solution meets the accuracy requirement.[67] Thus, eq 23 becomes

$$\frac{\partial^2 \xi_{D0}}{\partial r_D^2} + \frac{1}{r_D}\frac{\partial \xi_{D0}}{\partial r_D} = \omega\frac{\partial \xi_{D0}}{\partial t_D} + (1-\omega)\frac{\partial V_D}{\partial t_D} \tag{27}$$

Equation 27 is transformed into Laplace space as follows

$$\frac{d^2 \bar{\xi}_{D0}}{dr_D^2} + \frac{1}{r_D}\frac{d\bar{\xi}_{D0}}{dr_D} = \omega s\bar{\xi}_{D0} + (1-\omega)s\bar{V}_D \tag{28}$$

Combining the governing equation for the matrix block, i.e., eq 14, the coupling model for the matrix block and the natural fracture system can be written as follows

$$\frac{d^2 \bar{\xi}_{D0}}{dr_D^2} + \frac{1}{r_D}\frac{d\bar{\xi}_{D0}}{dr_D} = \{\omega s + 3\sigma\lambda(1-\omega)$$
$$[\sqrt{s/\lambda}\,\coth(\sqrt{s/\lambda}) - 1]\}\bar{\xi}_{D0} \tag{29}$$

where

$$f(s) = \omega s + 3\sigma\lambda(1-\omega)[\sqrt{s/\lambda}\,\coth(\sqrt{s/\lambda}) - 1] \tag{30}$$

So eq 29 can be expressed as follows

$$\frac{d^2 \bar{\xi}_{D0}}{dr_D^2} + \frac{1}{r_D}\frac{d\bar{\xi}_{D0}}{dr_D} = f(s)\bar{\xi}_{D0} \tag{31}$$

With boundary conditions in Laplace space

$$r_D\frac{\partial \bar{\xi}_{D0}}{\partial r_D}\bigg|_{r_D \to 0} = \bar{\bar{q}}_{fD} \tag{32}$$

$$\frac{\partial \bar{\xi}_{D0}}{\partial t_D}\bigg|_{r_D \to r_{eD}} = 0 \tag{33}$$

$$\bar{\xi}_{D0}|_{t=0} = 0 \tag{34}$$

So the dimensionless pseudopressure of the fracture system in the Laplace domain is

$$\bar{\xi}_{D0} = \bar{\bar{q}}_{fD}\left[K_0(r_D\sqrt{f(s)}) + \frac{I_0(r_D\sqrt{f(s)})K_1(r_{eD}\sqrt{f(s)})}{I_1(r_{eD}\sqrt{f(s)})}\right] \tag{35}$$

3.1.4. Pressure Response.
As a MFHW produces at a constant rate and the discrete unit number, n, is large enough, each discrete segment can be assumed as producing at a uniform flux density q_{ij}. The pressure response caused by the jth segment in the ith fracture can then be obtained by integrating eq 35.

$$\bar{\xi}_{Dij}(x_D, y_D) = \bar{\bar{q}}_{Dij}\int_{x_{Di,j}}^{x_{Di,j+1}}\left[K_0(r_D(x_D, y_D; x_{wD}, y_{wD})\sqrt{f(s)})\right.$$
$$+ \left.\frac{I_0(r_D(x_D, y_D; x_{wD}, y_{wD})\sqrt{f(s)})K_1(r_{eD}\sqrt{f(s)})}{I_1(r_{eD}\sqrt{f(s)})}\right]dx_{wDi} \tag{36}$$

where $r_D(x_D, y_D; x_{wD}, y_{wD}) = \sqrt{(x_D - x_{wD})^2 + (y_D - y_{wD})^2}$, in which $x_D = x/L_{ref}$, $y_D = y/L_{ref}$, $x_{wD} = x_w/L_{ref}$, and $y_{wD} = y_w/L_{ref}$. By applying the principle of superposition, the pressure responses at (x_D, y_D) caused by the $2n \times m$ segments can be estimated

$$\overline{\xi_{wD}} = \sum_{i=1}^{m} \sum_{j=1}^{2n} \overline{\xi_{Dij}}(\hat{x}_{Dk,v}, \hat{y}_{Dk,v}) \tag{37}$$

The well produces at a constant rate

$$\sum_{i=1}^{m} \sum_{j=1}^{2n} [\overline{\overline{q}}_{Dij} \Delta L_{fDij}] = \frac{1}{s} \tag{38}$$

Equations 37 and 38 consist a $(2n \times m + 1)$-order system of linear algebraic equations, which can be expressed in the following matrix form

$$\begin{bmatrix} A_{1*1,1*1} & \cdots & A_{1*1,k*k} & \cdots & A_{1*1,m*2n} & -1 \\ \cdots & \cdots & \cdots & \cdots & \cdots & -1 \\ A_{k*1,1*1} & \cdots & A_{k*1,k*k} & \cdots & A_{k*1,m*2n} & -1 \\ \cdots & \cdots & \cdots & \cdots & \cdots & -1 \\ A_{m*2n,1*1} & \cdots & A_{m*2n,k*k} & \cdots & A_{m*2n,m*2n} & -1 \\ \Delta L_{fD11} & \cdots & \Delta L_{fDij} & \cdots & \Delta L_{fDm2n} & 0 \end{bmatrix} \begin{bmatrix} \tilde{q}_{D11} \\ \cdot \\ \tilde{q}_{Dij} \\ \cdot \\ \tilde{q}_{Dm*2n} \\ \overline{\xi}_{wD} \end{bmatrix} = \begin{bmatrix} 0 \\ 0 \\ .. \\ .. \\ 0 \\ 1 \end{bmatrix} \tag{39}$$

$$A_{i*j,k*v} = \int_{y_{Di,j}}^{y_{Di,j+1}} \left[K_0\left(\sqrt{(x_{Dk*v} - x_{Di*j})^2 + (y_{Dk*v} - \xi)^2} \sqrt{f(s)} \right) \right.$$
$$\left. + \frac{I_0\left(\sqrt{(x_{Dk*v} - x_{Di*j})^2 + (y_{Dk*v} - \xi)^2} \sqrt{f(s)} \right) K_1(r_{eD}\sqrt{f(s)})}{I_1(r_{eD}\sqrt{f(s)})} \right] d\xi \tag{40}$$

where $A_{i*j,k*v}$ is the coefficient of pseudopressure drop of the vth discrete unit of the kth fracture caused by a continuous line source of unit strength at the jth discrete unit of the ith fracture.

From eq 22, the bottom-hole pressure for MFHW in stress-sensitive shale gas reservoirs is given by

$$\overline{\psi}_{wDH}(t_D) = -\frac{1}{\gamma_D - \delta_D} \ln[1 - (\gamma_D + \delta_D)\overline{\xi}_{wDH}(t_D)] \tag{41}$$

3.1.5. Production Solution. Based on Van Everdingen and Hurst's study,[68,69] the relationship between dimensionless production at constant bottom-hole pressure and dimensionless bottom pseudopressure at a constant production rate is expressed as follows

$$\overline{q}_{wD}(s) = \frac{1 - e^{[-(\gamma_D + \delta_D)]}}{\gamma_D + \delta_D} \frac{1}{s^2} \frac{1}{\overline{\psi}_{wDH}(s)} \tag{42}$$

From the Stehfest numerical inversion algorithm, dimensionless production in real-time space, q_D, can be obtained by eqs 43−45

$$q_D(t_D) = \frac{\ln 2}{t} \sum_{i=1}^{N} V_i \overline{q}_D(s) \tag{43}$$

$$s = i\frac{\ln 2}{t} \tag{44}$$

$$V_i = (-1)^{N/2+1}$$
$$\sum_{k=[\frac{i+1}{2}]}^{\min(i,\frac{N}{2})} \frac{k^{N/2}(2k)!|^{s=i^{\ln 2/t}}}{\left(\frac{N}{2} - k\right)!k!(k-1)!(i-k)!(2k-i)!} \tag{45}$$

Then, the production rate can be expressed as follows

$$q_{sc} = \frac{\pi k_{fi} h T_{sc}(\psi_{fi} - \psi_{wf})}{p_{sc}} q_D \tag{46}$$

3.2. Database Collection. The proposed model in this study was applied to the Marcellus shale play. As the national leader in shale gas production, the Marcellus shale play is the source of more than 18% dry gas production in the United States. The area that has dry gas resources is mainly in the northeast of the Marcellus shale play. Susquehanna County is picked out as the target area. From open data sources (Drillinginfo, 2021), over 1001 shale wells have been horizontally drilled in Susquehanna County. To conveniently analyze the production, the wells were divided into three well groups: low productive wells, medium productive wells, and high productive wells, with average production rates of less than 50 000 Mscf/month, between 50 000 and 200 000 Mscf/month, and higher than 200 000 Mscf/month, respectively. Some details are shown in Table 2. In this article, the high productive well group has 123 single wells, as shown in Figure 4. The average rate data versus time of these wells is plotted, as shown in Figure 5. From Figure 5, the whole production process can be divided into three stages, namely, increasing, rapid decline, and persistent decline periods. The increasing production period is called flowback, which is a two-phase (gas and water) flow. After flowback, the next two production periods, namely, the rapid decline and persistent decline periods have only gas flowing. The model proposed in this article is suitable for dry gas reservoirs. Therefore, the last two periods are chosen for analysis.

3.3. Model Verification. The entire set of coupled equations, as presented in Section 3.1, was programmed and solved using MATLAB. The reservoir and engineering parameters were obtained from Drillinginfo 2021, and the values of these parameters were averaged for the synthetic model, and are listed in Table 2. The average production rate of the high productive well group was picked as an example to show the workflow analysis. This model is suitable for dry shale gas. Therefore, the decline and persistent decline periods were chosen for analysis.

The stress-sensitive permeability model only considers permeability as a stress-sensitive parameter. In the new model, two more stress-sensitive parameters (porosity and diffusivity) are considered. From Figure 6, the new model proposed in this article had a very good fit with field data. Meanwhile, a model with permeability as the only sensitive parameter is compared with the proposed new model in this article. Compared with the new model, the stress-dependent permeability model declines faster during the rapid decline production period. Moreover, the difference between these two models became larger as depletion continued. It is known that pore pressure declines with the continuous production so diffusivity is larger with the decline of pressure. It indicates that the velocity of gas diffusion increases with the pressure decline and there is more gas supply in the new model. Thus, sensitive diffusion can counteract the damage caused by stress-dependent permeability. Overall, the new model had a good match with the field data and was more reasonable as it considered multiple stress-sensitive parameters.

3.4. Sensitivity Analysis. This subsection shows how reservoir and some model parameters affect the decline curves. The sensitivity analysis focuses on the rapid decline and
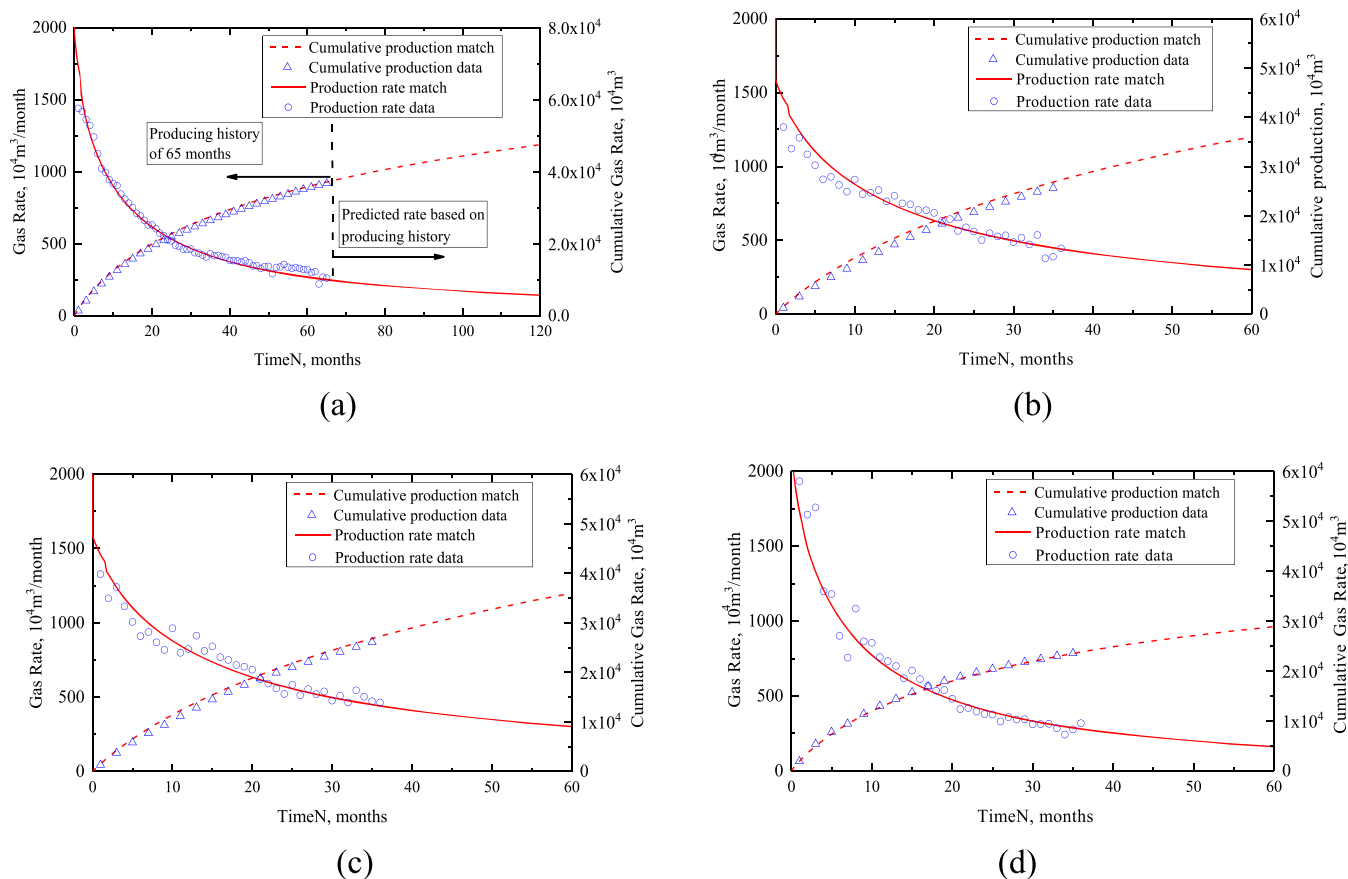
Figure 11. Comparison of production curves between stress dependence of permeability and reservoir (including permeability, porosity, and diffusivity)-high productivity well group: (a) high productivity well group, (b) well GRASAVAGE E-2, (c) well GRASAVAGE E-4, and (d) well MAKOSKY T-8.

persistent decline periods. The base-case data set shown in Tables 3 and 2 is substituted into the synthetic model to obtain the production rate curve.

It is observed from Figure 7 that initial diffusivity affected almost the entire producing period. During the early production period, majority of produced gas comes from free gas. Therefore, the initial production rate was barely affected by initial diffusivity. However, when desorption and diffusion dominated due to Langmuir pressure, there was a gentle decline in the production rate curve, and cumulative production increased with higher values of initial diffusivity.

It can be seen from Figure 8 that initial porosity of natural fractures affected almost the entire production period. There was no apparent relationship between the initial production rate and initial porosity. The reasons attributed to the effect of initial permeability of natural fractures on the production rate and cumulative production holds for that of initial porosity. With higher initial porosity of natural fractures, the rate of production decline became slower. Free gas in macroscale pores is the main source of gas production during the early production period. Therefore, there was more gas stored in the effective pores with higher initial natural fracture porosity. However, the difference in production and decline rates among the three conditions (ϕ_i = 0.001, 0.002, 0.003) decreased. This is because desorption on the surface of kerogen and diffusion in nano- and microscale pores dominated the persistent decline production period.

It is observed from Figure 9 that initial permeability of natural fracture mainly affected the rapid decline period. Majority of early produced gas comes from free gas when the seepage flow in macroscale pores dominates. Thus, with higher values of natural facture initial permeability, the initial production rate was higher and the decline in the production rate became slower. Moreover, cumulative production was higher with higher initial permeability.

From Figure 10, a dimensionless sensitive modulus is the difference in the value between dimensionless sensitive permeability and diffusivity modulus. It affected almost the entire production stages. As shown in Figure 3, diffusivity is larger with the decline of pressure. It indicates that more and more desorption gas diffuse into the fracture system with gas supply. Thus, sensitive diffusion can counteract the damage caused by stress-dependent permeability. A higher dimensionless sensitive modulus represents a higher velocity of fracture closure and accordingly, a slow increase in diffusivity leading to less desorption gas production. Therefore, the production rate reduced and the rate of decline was more rapid with a higher value of the dimensionless sensitive modulus.

4. RESULTS

The field example presented in this paper is three well groups of MFHW drilled in the dry gas reservoir of the Marcellus Shale. Three single MFHWs of each well group have also been picked out and analyzed to confirm the proposed model's applicability. The average gas production rate of well groups
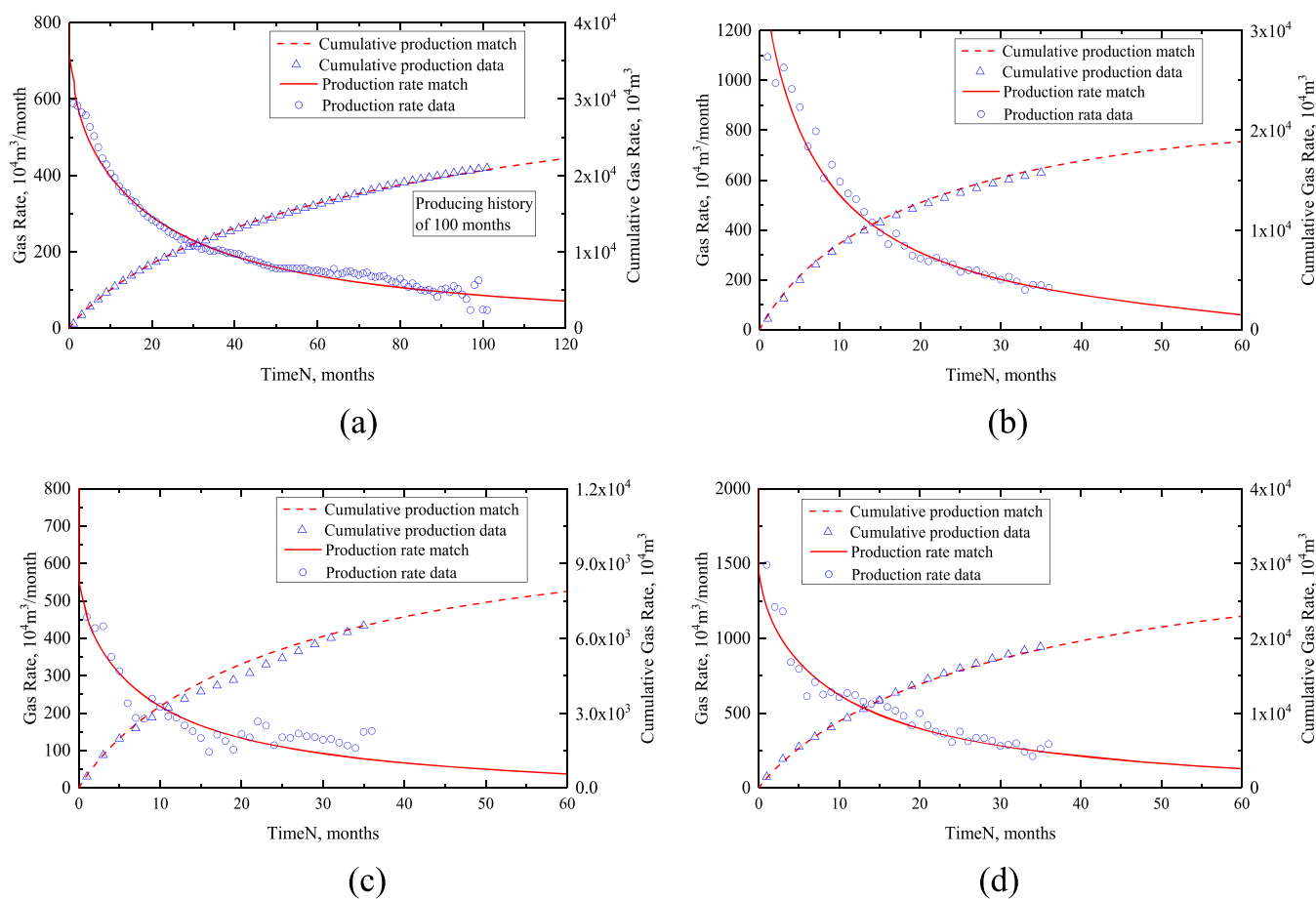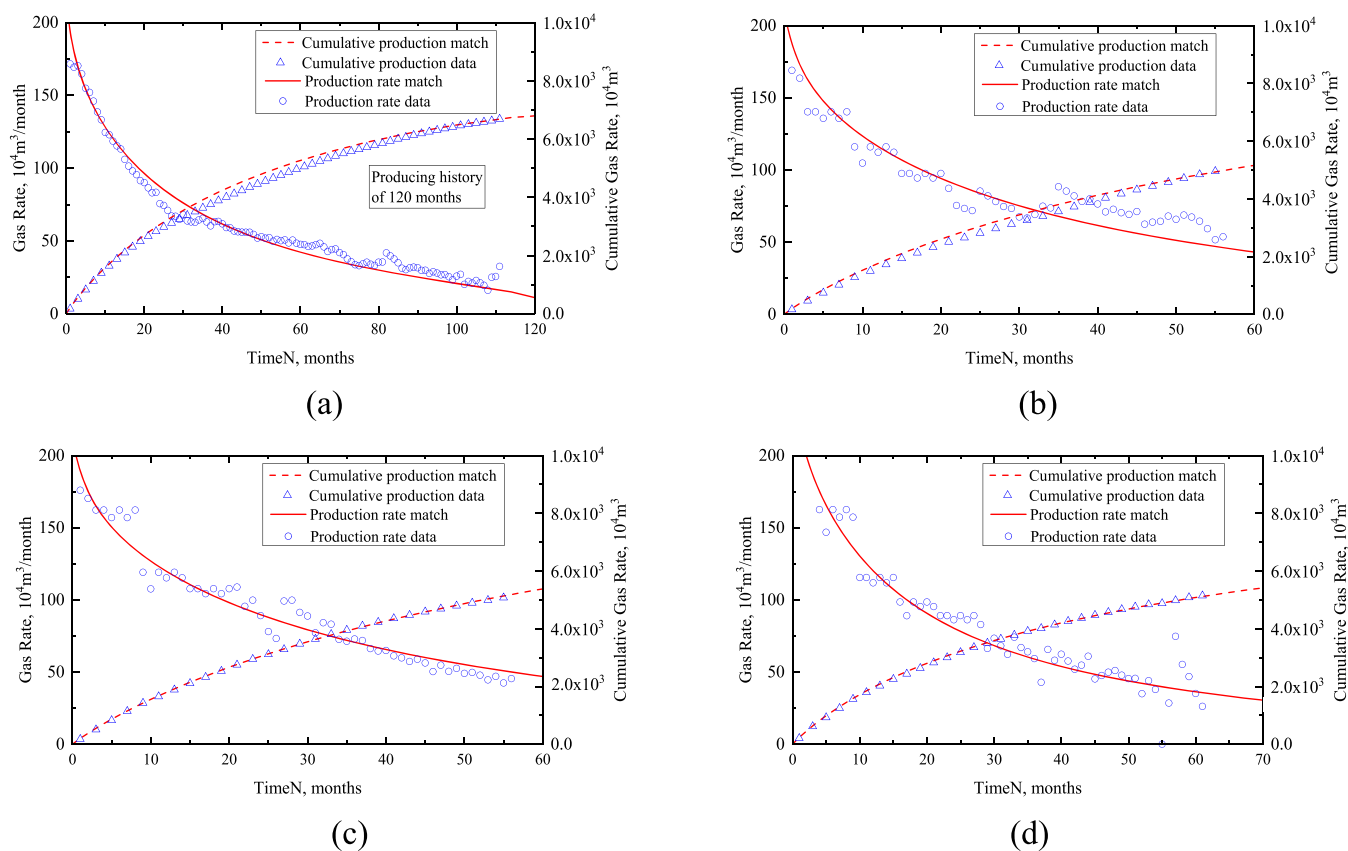
Figure 12. Comparison of production curves between stress dependence of permeability and reservoir (including permeability, porosity, and diffusivity)-medium productivity well group: (a) medium productivity well group, (b) well LATHROP FARM TRUST UNIT B-1H, (c) well LATHROP FARM TRUST UNIT B-3H, and (d) well MAKOSKY T-1.

with a constant bottom-hole pressure condition can be seen in Figures 11a, 12a, and 13a. Production data were extracted from only the rapid and persistent decline periods for analysis as the proposed model is only suitable for dry gas. The values of some basic parameters are shown in Table 2, and the inverse results are shown in Table 4. It can be seen that the results from the proposed model and the production rate history of these three well groups are perfectly matched.

Figure 11a shows the modeling results and field data for the high productive well group. This well group has almost 65 months of production history. There was a good match between the proposed model and field data. The reservoir parameters (k_{fi} = 1.1 × 10^{-16} m^2, D_i = 3 × 10^{-11} m^2/s, ϕ_i = 0.001, $\gamma_D - \delta_D$ = 0.01, h = 80 m) and treatment scale parameters (L = 2000 m, M = 20, x_f = 150 m, r_e = 635 m) were obtained by inversion. Similarly, three representative single wells were chosen and fitted with field data. The results of the modeling are shown in Figure 11b−d. The initial permeability of natural fractures varied from 0.9 × 10^{-16} m^2 to 1.3 × 10^{-16} m^2, while the average value was 1.1 × 10^{-16} m^2 for the high productive well group. The initial diffusivity and initial porosity of the well group and single wells were the same, and these values were 3 × 10^{-11} m^2 and 0.001, respectively. The total dimensionless sensitive modulus varied from 0.01 to 0.05, while the average value was 0.01. Fracture half-lengths and effective heights were all equal to 150 and 80 m, respectively. The inverted parameters are listed in Table 4.

Figure 12a shows the modeling results and field data for the medium productive well group. This well group has 100 months of production history. There was a good match between the proposed model and field data. The reservoir parameters (k_{fi} = 0.55 × 10^{-16} m^2, D_i = 3 × 10^{-11} m^2/s, ϕ_i = 0.001, $\gamma_D - \delta_D$ = 0.05, h = 60 m) and treatment scale parameters (L = 1600 m, M = 16, x_f = 150 m, r_e = 572 m) were obtained by inversion. Similarly, three representative single wells were chosen and fitted with field data. The results of the modeling are shown in Figure 12b−d. The initial permeability of natural fractures varied from 0.6 × 10^{-16} m^2 to 1.1 × 10^{-16} m^2, while the basic value was 0.55 × 10^{-16} m^2 for the medium productive well group. The initial diffusivity and initial porosity of the well group and single wells were the same, and these values were 3 × 10^{-11} m^2 and 0.001, respectively. The total dimensionless sensitive modulus was 0.01, while the basic value was 0.05. The fracture half-length ranged from 130 to 180 m, while the basic value was 150 m. The effective height varied from 45 to 70 m, while the basic value was equal to 60 m. The inverted parameters are listed in Table 4.

Figure 13a shows the modeling results and field data for the low productive well group. This well group has 110 months of production history. There was a good match between the proposed model and field data. The reservoir parameters (k_{fi} = 0.35 × 10^{-16} m^2, D_i = 3 × 10^{-11} m^2/s, ϕ_i = 0.001, $\gamma_D - \delta_D$ = 0.18, h = 30 m) and treatment scale parameters (L = 1400m, M = 14, x_f = 150 m, r_e = 538 m) were obtained by inversion.

Figure 13. Comparison of production curves between stress dependence of permeability and reservoir (including permeability, porosity, and diffusivity)-low productivity well group: (a) low productivity well group, (b) well CARRAR-2H, (c) well HAYES-1-6H, and (d) well IVEY-1H.

Table 4. Values of Different Well Groups

| well group	well name	k_{fi}, m^2	D_i, m^2/s	ϕ_i	$\gamma_D - \delta_D$	L, m	x_f, m	r_e, m	h, m
high productive	basic values	1.1×10^{-16}	3×10^{-11}	0.001	0.01	2000	150	635	80
	GRASAVAGE E-2	0.9×10^{-16}	3×10^{-11}	0.001	0.01	2400	150	693	80
	GRASAVAGE E-4	0.9×10^{-16}	3×10^{-11}	0.001	0.01	2400	150	693	80
	MAKOSKY T-8	1.3×10^{-16}	3×10^{-11}	0.001	0.05	1400	150	538	80
medium productive	basic values	0.55×10^{-16}	3×10^{-11}	0.001	0.05	1600	150	572	60
	LATHROP FARM TRUST UNIT B-1H	1.1×10^{-16}	3×10^{-11}	0.001	0.1	900	180	488	70
	LATHROP FARM TRUST UNIT B-3H	0.6×10^{-16}	3×10^{-11}	0.001	0.1	900	130	407	45
	MAKOSKY T-1	1×10^{-16}	3×10^{-11}	0.001	0.1	1300	180	574	70
low productive	basic values	0.35×10^{-16}	3×10^{-11}	0.001	0.18	1400	150	538	30
	CARRAR-2H	0.35×10^{-16}	3×10^{-11}	0.001	0.18	1900	120	551	30
	HAYES-1-6H	0.35×10^{-16}	3×10^{-11}	0.001	0.18	1900	130	575	30
	IVEY-1H	0.4×10^{-16}	3×10^{-11}	0.001	0.1	1000	140	444	30

Similarly, three representative single wells were chosen and fitted with field data. The results of the modeling are shown in Figure 13b−d. The initial permeability of natural fractures varied from 0.35×10^{-16} m^2 to 0.4×10^{-16} m^2, while the basic value was 0.35×10^{-16} m^2 for the low productive well group. The initial diffusivity and initial porosity of the well group and single wells were the same, and these were 3×10^{-11} m^2 and 0.001, respectively. The total dimensionless sensitive modulus varied from 0.1 to 0.18, while the basic value was 0.18. The fracture half-length varied from 120 to 140 m, while the basic value was 150 m. Effective heights were all equal to 30 m. The inverted parameters are listed in Table 4.

The initial diffusivity and porosity of natural fractures were all same, and these values were 3×10^{-11} m^2/s and 0.001, respectively. Horizontal lengths were from drilling and completion data. From Table 4, the rest of the parameters were strongly related to the basic values, i.e., the inverted parameter values varied as the basic value changed. This serves as a guideline for dynamic analysis in shale gas reservoirs.

5. DISCUSSION

The results of this study can be summarized under five points, namely, (1) the development of a mathematical model for stress-sensitive shale gas reservoirs, (2) the derivation of the production rate as an explicit function of reservoir and treatment parameters, (3) the proposition of a workflow for rate transient analysis, (4) implementation of sensitivity analysis, and (5) the application of this workflow to history match of the Marcellus shale.
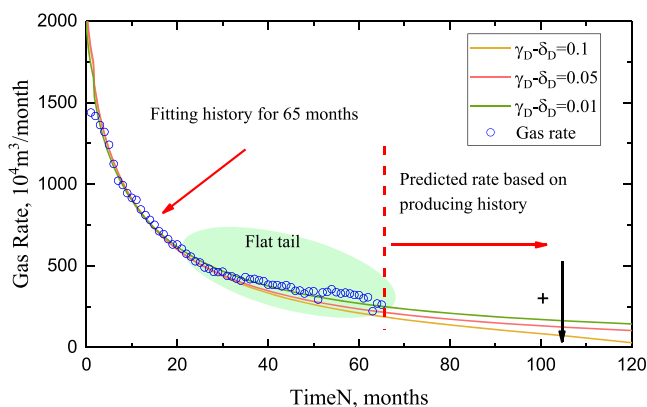
Figure 14. Impact of sensitive parameters on the rate decline curves ($\gamma_D - \delta_D = 0.01$: $k_{fi} = 1.1 \times 10^{-16}$ m^2, $\phi = 0.001$, $D_i = 3.08 \times 10^{-13}$ m^2/s; $\gamma_D - \delta_D = 0.05$: $k_{fi} = 1.2 \times 10^{-16}$ m^2, $\phi = 0.001$, $D_i = 3.08 \times 10^{-13}$ m^2/s; $\gamma_D - \delta_D = 0.01$: $k_{fi} = 1.2 \times 10^{-16}$ m^2, $\phi = 0.003$, $D_i = 3.08 \times 10^{-13}$ m^2/s).

The entire production process can be divided into three stages: increasing (flowback) period, rapid decline, and persistent decline periods. Water and gas two-phase flow occured during the increasing (flowback) period of the production, while only gas flowed during the rapid decline and persistent decline periods. However, there was a "flat tail" during the persistent production period, as shown in Figure 14. This was mainly caused by increased diffusion and desorption. The results of the modeling indicated that the production rate declined more slowly with smaller values of the total dimensionless sensitive modulus. The total dimensionless sensitive modulus reduced as the diffusivity-sensitive modulus was added. Therefore, considering diffusivity as a stress-independent parameter resulted in a better explicit and applicable rate transient analytical model. Even if the green line ($\gamma_D - \delta_D = 0.01$) approached the field data, the trend of the field data curve would still be upward.

6. CONCLUSIONS

This work examined rate transient analysis of MFHW in stress-sensitive shale gas reservoirs by incorporation of multiple stress-dependent parameters. Based on the results, several conclusions are drawn as follows:

(1) The proposed semianalytical production model can be used to predict the long-term gas production behavior. The inclusion of stress-dependent diffusivity, porosity, and permeability of shale gas reservoirs ensured that the model could predict the long-term production behavior, especially during the late production stage. Moreover, multiple stress-dependent parameters resulted in strong nonlinearities of the governing equation. This problem was solved by employing a perturbation method to weaken the strong nonlinearities.

(2) Meanwhile, the rate transient model with multiple stress-dependent parameters had a slower decline compared to the model with only stress-dependent permeability. This was attributed to the fact that desorption and diffusion became increasingly pronounced during depletion. As pressure was depleted, diffusivity increased. Moreover, diffusion occured in the later stages of depletion. Therefore, the impact of stress-dependent diffusivity on the production rate was crucial during the late

production period. The results of the model were identical with the production data where both had a flat tail.

(3) Overall, 1001 wells from the Marcellus shale play were selected to verify the validity of the proposed model. To conveniently analyze the production data, these wells were divided into three well groups: low productive well group, medium productive well group, and high productive well group. Three wells of each well group were picked out for production rate analysis. Moreover, the initial diffusivity (3×10^{-11} m^2/s) and initial porosity (0.001) of the natural fractures were all same. Meanwhile, horizontal well lengths were from drilling and completion data. The values of inverted parameters of single wells changed within the basic values of well groups. This indicates that modeling and inverting well groups could serve as a guideline for single-well dynamic analysis in shale gas reservoirs.

■ APPENDIX

The dimensionless equations for the transient diffusion model for the matrix are expressed as follows based on Section 3.1.1.

$$\frac{\partial V_D}{\partial t_D} = 3\lambda \frac{\partial V_D}{\partial r_{mD}}\bigg|_{r_{mD}=1} \tag{A1}$$

$$\frac{1}{r_{mD}^2} \frac{\partial}{\partial r_{mD}}\left(r_{mD}^2 \frac{\partial V_D}{\partial r_{mD}}\right) = \frac{1}{\lambda}\frac{\partial V_D}{\partial t_D} \tag{A2}$$

$$\frac{\partial V_D}{\partial r_{mD}}\bigg|_{r_{mD}\to 0} = 0 \tag{A3}$$

$$V_D|_{r_{mD}=1} = V_{ED} \tag{A4}$$

$$V_D|_{t_D=0} = 0 \tag{A5}$$

where $\lambda = \frac{\mu_i \Lambda L_{ref}^2}{k_i \tau}$, $\tau = \frac{R_m^2}{D}$, $r_{mD} = \frac{r_m}{R_m}$, $V_{ED} = V_i - V_E$. Taking Laplace transformations of eqs A1−A5 yields

$$s\bar{V}_D = 3\lambda \frac{d\bar{V}_D}{dr_{mD}}\bigg|_{r_{mD}=1} \tag{A6}$$

$$\frac{1}{r_{mD}^2} \frac{\partial}{\partial r_{mD}}\left(r_{mD}^2 \frac{\partial \bar{V}_D}{\partial r_{mD}}\right) = \frac{1}{\lambda}s\bar{V}_D \tag{A7}$$

$$\frac{d\bar{V}_D}{dr_{mD}}\bigg|_{r_{mD}\to 0} = 0 \tag{A8}$$

$$\bar{V}_D|_{r_{mD}=1} = \bar{V}_{ED} \tag{A9}$$

eq A7 becomes by making

$$\bar{E} = r_{mD}\bar{V}_D \frac{d^2\bar{E}}{dr_{mD}^2} - \frac{s}{\lambda}\bar{E} = 0 \tag{A10}$$

The general solution of eq A10 is as follows

$$E = A_1 e^{-\sqrt{s/\lambda}\, r_{mD}} + A_2 e^{\sqrt{s/\lambda}\, r_{mD}} \tag{A11}$$

Then,

$$\bar{V}_{\mathrm{D}} = A_1 \frac{e^{-\sqrt{s/\lambda}\,r_{\mathrm{mD}}}}{r_{\mathrm{mD}}} + A_2 \frac{e^{\sqrt{s/\lambda}\,r_{\mathrm{mD}}}}{r_{\mathrm{mD}}} \tag{A12}$$

Substituting eq A12 into eq A8 yields

$$\left.\frac{d\bar{V}_{\mathrm{D}}}{dr_{\mathrm{mD}}}\right|_{r_{\mathrm{mD}}\to 0} = A_1 \frac{-\sqrt{s/\lambda}\;e^{-\sqrt{s/\lambda}\,r_{\mathrm{mD}}}r_{\mathrm{mD}} - e^{-\sqrt{s/\lambda}\,r_{\mathrm{mD}}}}{r_{\mathrm{mD}}^2}$$
$$+ A_2 \frac{\sqrt{s/\lambda}\;e^{-\sqrt{s/\lambda}\,r_{\mathrm{mD}}}r_{\mathrm{mD}} - e^{-\sqrt{s/\lambda}\,r_{\mathrm{mD}}}}{r_{\mathrm{mD}}^2} \tag{A-13}$$

The following relationship can be obtained combining the inner boundary condition eq A13

$$A_2 = -A_1 \tag{A14}$$

Then, eq A12 can be expressed as

$$\bar{V}_{\mathrm{D}} = A_1 \left(\frac{e^{-\sqrt{s/\lambda}\,r_{\mathrm{mD}}}}{r_{\mathrm{mD}}} - \frac{e^{\sqrt{s/\lambda}\,r_{\mathrm{mD}}}}{r_{\mathrm{mD}}} \right) \tag{A15}$$

Substituting eq A15 into eq A9 yields

$$\bar{V}_{\mathrm{ED}} = A_1(e^{-\sqrt{s/\lambda}} - e^{\sqrt{s/\lambda}}) \tag{A16}$$

After taking Laplace transformation with respect to t_{D}, eq 27 can be further rewritten as follows

$$\bar{V}_{\mathrm{ED}} = \sigma \bar{\psi}_{\mathrm{D}} \tag{A17}$$

Combining eqs A16 and A17 yields

$$A_1 = \frac{\sigma}{(e^{-\sqrt{s/\lambda}} - e^{\sqrt{s/\lambda}})}\bar{\psi}_{\mathrm{D}} \tag{A18}$$

The dimensionless gas concentration in a shale matrix in the Laplace space can be obtained by substituting eq A18 into eq A15

$$\bar{V}_{\mathrm{D}} = \frac{\sigma}{sh(\sqrt{s/\lambda})} \frac{sh(\sqrt{s/\lambda}\,r_{\mathrm{mD}})}{r_{\mathrm{mD}}}\bar{\psi}_{\mathrm{D}} \tag{A19}$$

where $sh(\sqrt{s/\lambda})$ is the hyperbolic sine function.

Equation A19 can be further derived as follows

$$\left.\frac{\partial \bar{V}_{\mathrm{D}}}{\partial r_{\mathrm{mD}}}\right|_{r_{\mathrm{mD}}=1} = \sigma[\sqrt{s/\lambda}\,\coth\sqrt{s/\lambda} - 1]\bar{\psi}_{\mathrm{D}} \tag{A20}$$

Thus, eq 6 can be rewritten as

$$s\bar{V}_{\mathrm{D}} = 3\lambda\left.\frac{d\bar{V}_{\mathrm{D}}}{dr_{\mathrm{mD}}}\right|_{r_{\mathrm{mD}}=1} = 3\sigma\lambda[\sqrt{s/\lambda}\,\coth\sqrt{s/\lambda} - 1]\bar{\psi}_{\mathrm{D}} \tag{A21}$$

■ AUTHOR INFORMATION

Corresponding Author

Ting Lu − *SINOPEC Key Laboratory of Shale Oil/Gas Exploration & Production, Beijing 100083, China;* ⓞ orcid.org/0000-0001-5459-958X; Phone: +8618310901966; Email: luting2019.syky@sinopec.com

Authors

Shengxiang Long − *SINOPEC Key Laboratory of Shale Oil/ Gas Exploration & Production, Beijing 100083, China*

Zhiping Li − *School of Energy Resource, China University of Geosciences (Beijing), Beijing 100083, China*

Shimin Liu − *Department of Energy and Mineral Engineering, G³ Center and Energy Institute, The Pennsylvania State University, University Park, Pennsylvania 16802, United States;* ⓞ orcid.org/0000-0001-9612-0047

Yu Liu − *China University of Mining and Technology, Beijing 100083, China*

Caspar Daniel Adenutsi − *Department of Petroleum Engineering, Faculty of Civil and Geo-Engineering, Kwame Nkrumah University of Science and Technology, Kumasi, Ghana*

Zeyang Peng − *SINOPEC Key Laboratory of Shale Oil/Gas Exploration & Production, Beijing 100083, China*

Notes

The authors declare no competing financial interest.

■ ACKNOWLEDGMENTS

■ NOMENCLATURE

B_{g}	volume factor, dimensionless
C	wellbore storage coefficient, m³/Pa
C_{D}	dimensionless wellbore storage coefficient, dimensionless
C_{g}	gas compressibility, Pa⁻¹
C_{gi}	gas compressibility at initial condition, Pa⁻¹
D	diffusion coefficient, m²/s
h	reservoir thickness, m
k_{m}	permeability of the matrix system, m²
k_{fi}	permeability of the fracture system at initial condition, m²
$I_0(x)$	modified Bessel function of first kind, zero order
$K_0(x)$	modified Bessel function of second kind, zero order
$K_1(x)$	modified Bessel function of second kind, first order
L_{ref}	reference length, m
L_{h}	length of horizontal well
M	number of hydraulic fractures
M_{g}	apparent molecular weight of shale gas, kg/kmol
n	molar quantity of shale gas, kmol
p	pressure of the fracture system, Pa
pi	initial pressure of shale gas reservoirs, Pa
p_{sc}	pressure at standard condition, Pa
$\hat{q}(t)$	surface production rate of the line sink, m³/s
q^*	mass flow rate per unit reservoir between the shale matrix and fracture, kg/(m³·s)
q_{ij}	flux density of the jth segment in the ith fracture, m³/(s·m)
$\bar{q}_{ij}(s)$	Laplace transformation of q_{ij}
q_{sf}	sandsurface flow rate, m³/s
$\hat{q}_{\mathrm{D}}$	dimensionless production rate of the line sink, dimensionless
r	radial radius, m
r_{m}	radial radius in spherical matrix blocks, m
r_{w}	well radius of multiple fractured horizontal well, m

r_D	dimensionless radius, dimensionless
R	gas constant, J/(mol·K)
R_m	external radius of the matrix block, m
δ_D	dimensionless porosity modulus, dimensionless
S	skin factor, dimensionless
t	time, s
t_D	dimensionless time, dimensionless
T	reservoir temperature, K
T_{sc}	temperature at standard condition, K
v	flow velocity of shale gas in the fracture system, m/s
V	volumetric gas concentration, sm^3/m^3
V_D	dimensionless gas concentration, dimensionless
V_E	equilibrium volumetric gas concentration, sm^3/m^3
V_i	volumetric gas concentration at initial condition, sm^3/m^3
V_L	Langmuir volume (at standard condition), sm^3/m^3
x, y	x- and y-coordinates, m
y_i	y-coordinate of the intersection of the ith fracture and y-axis, m
Δy_i	difference between y_i and y_{i-1}
X_{fU_i}	length of upper wing of ith fracture, m
X_{fL_i}	length of lower wing of ith fracture, m
$\Delta X_{f_{ij}}$	length of discrete segment (i, j), m
$\Delta X_{fD_{ij}}$	dimensionless length of discrete segment (i, j), dimensionless
Z	Z-factor of shale gas, dimensionless
p	shale gas density, kg/m^3
ρ_{sc}	shale gas density at standard condition, kg/m^3
ϕ	porosity, fraction gas viscosity, Pa·s
μ_g	gas viscosity at initial condition, Pa·s
σ	adsorption index, dimensionless
β	a parameter related to permeability modulus, Pa^{-1}·s
ψ	pseudopressure, Pa/s
ψ_L	Langmuir pseudopressure, Pa/s
ψ_i	pseudopressure at initial condition, Pa/s
$\Delta\psi$	pseudopressure difference, Pa/s
$\Delta\psi_s$	additional pseudopressure drop, Pa/s
ψ_D	dimensionless pseudopressure, dimensionless
ω	storativity ratio, dimensionless
λ	interporosity flow coefficient, dimensionless total storage capacity, Pa^{-1}
γ_D	dimensionless permeability modulus, dimensionless

■ REFERENCES

(1) Dong, Z.; Holditch, S.; McVay, D. Resource Evaluation for Shale Gas Reservoirs. *SPE Econ. Manage.* **2013**, *5*, 5−16.

(2) Alkouh, A. New Advances in Shale Gas Reservoir Analysis Using Water Flowback Data. Doctoral Dissertation, Texas A&M University, 2014.

(3) Roy, S.; Raju, R.; Chuang, H. F.; Cruden, B. A.; Meyyappan, M. Modeling Gas Flow through Microchannels and Nanopores. *J. Appl. Phys.* **2003**, *93*, 4870−4879.

(4) Civan, F. Effective Correlation of Apparent Gas Permeability in Tight Porous Media. *Transp. Porous Media* **2010**, *82*, 375−384.

(5) Sakhaee-Pour, A.; Bryant, S. Gas Permeability of Shale. *SPE Reserv. Eval. Eng.* **2012**, *15*, 401−409.

(6) Ma, L.; Slater, T.; Dowey, P. J.; Yue, S.; Rutter, E. H.; Taylor, K. G.; Lee, P. D. Hierarchical Integration of Porosity in Shales. *Sci. Rep.* **2018**, *8*, No. 1683.

(7) Warren, J. E.; Root, P. J. The Behavior of Naturally Fractured Reservoirs. *Soc. Pet. Eng. J.* **1963**, *3*, 245−255.

(8) Wang, Y.; Zhu, Y.; Liu, S.; Zhang, R. Pore Characterization and Its Impact on Methane Adsorption Capacity for Organic-Rich Marine Shales. *Fuel* **2016**, *181*, 227−237.

(9) Al-Hussainy, R.; Ramey, H. J.; Crawford, P. B. The Flow of Real Gases through Porous Media. *J. Pet. Technol.* **1966**, *18*, 624−636.

(10) Javadpour, F.; Fisher, D.; Unsworth, M. Nanoscale Gas Flow in Shale Gas Sediments. *J. Can. Pet. Technol.* **2007**, *46*, 55−61.

(11) Zhang, R.; Liu, S.; Wang, Y. Fractal Evolution under in Situ Pressure and Sorption Conditions for Coal and Shale. *Sci. Rep.* **2017**, *7*, No. 8971.

(12) Bumb, A. C.; McKee, C. R. Gas-Well Testing in the Presence of Desorption for Coalbed Methane and Devonian Shale. *SPE Form. Eval.* **1988**, 179−185.

(13) Mengal, S. A.; Wattenbarger, R. A. In *Accounting for Adsorbed Gas in Shale Gas Reservoirs*, SPE Middle East Oil and Gas Show and Conference, Society of Petroleum Engineers, 2011; pp 643−657.

(14) Shabro, V.; Javadpour, F. In *Numerical Simulation of Shale-Gas Production: From Pore-Scale Modeling of Slip-Flow, Knudsen Diffusion, and Langmuir Desorption to Reservoir Modeling of Compressible Fluid*, North American Unconventional Gas Conference and Exhibition, 2011; pp 1−11.

(15) Haghshenas, B.; Clarkson, C. R.; Chen, S. In *Multi-Porosity, Multi-Permeability Models for Shale Gas Reservoirs*, SPE Unconventional Resources Conference Canada, 2013.

(16) Lu, X. C.; Li, F. C.; Watson, A. T. Adsorption Measurements in Devonian Shales. *Fuel* **1995**, *74*, 599−603.

(17) Weniger, P.; Kalkreuth, W.; Busch, A.; Krooss, B. M. High-Pressure Methane and Carbon Dioxide Sorption on Coal and Shale Samples from the Paraná Basin, Brazil. *Int. J. Coal Geol.* **2010**, *84*, 190−205.

(18) Hu, H.; Zhang, T.; Wiggins-Camacho, J. D.; Ellis, G. S.; Lewan, M. D.; Zhang, X. Experimental Investigation of Changes in Methane Adsorption of Bitumen-Free Woodford Shale with Thermal Maturation Induced by Hydrous Pyrolysis. *Mar. Pet. Geol.* **2015**, *59*, 114−128.

(19) Guo, H.; Jia, W.; Peng, P.; Zeng, J.; He, R. Evolution of Organic Matter and Nanometer-Scale Pores in an Artificially Matured Shale Undergoing Two Distinct Types of Pyrolysis: A Study of the Yanchang Shale with Type II Kerogen. *Org. Geochem.* **2017**, *105*, 56−66.

(20) Xiao, J.; Wei, J. Diffusion of Hydrocarbons Theory. *Chem. Eng. Sci.* **1992**, *47*, 1123−1141.

(21) Fathi, E.; Akkutlu, I. Y. Lattice Boltzmann Method for Simulation of Shale Gas Transport in Kerogen. *SPE J.* **2013**, *18*, 27−37.

(22) Wua, K.; Li, X.; Guo, C.; Chen, Z. In *Adsorbed Gas Surface Diffusion and Bulk Gas Transport in Nanopores of Shale Reservoirs with Real Gas Effect-Adsorption-Mechanical Coupling*, SPE Reservoir Simulation Symposium, 2015; pp 1−30.

(23) Javadpour, F. Nanopores and Apparent Permeability of Gas Flow in Mudrocks (Shales and Siltstone). *J. Can. Pet. Technol.* **2009**, *48*, 16−21.

(24) Kikani, J.; Pedrosa, O. A., Jr Perturbation Analysis of Stress-Sensitive Reservoirs. *SPE Form. Eval.* **1991**, *6*, 379−386.

(25) Wang, Y.; Liu, S. Estimation of Pressure-Dependent Diffusive Permeability of Coal Using Methane Diffusion Coefficient: Laboratory Measurements and Modeling. *Energy Fuels* **2016**, *30*, 8968−8976.

(26) Fan, L.; Liu, S. A Novel Experimental System for Accurate Gas Sorption and Its Application to Various Shale Rocks. *Chem. Eng. Res. Des.* **2021**, *165*, 180−191.

(27) Liu, J.; Wang, J. G.; Gao, F.; Ju, Y.; Zhang, X.; Zhang, L. Flow Consistency Between Non-Darcy Flow in Fracture Network and Nonlinear Diffusion in Matrix to Gas Production Rate in Fractured Shale Gas Reservoirs. *Transp. Porous Media* **2016**, *111*, 97−121.

(28) Soeder, D. J. Porosity and Permeability of Eastern Devonian Gas Shale. *SPE Form. Eval.* **1988**, *3*, 116−124.

(29) Davies, D. K.; Bryant, W. R.; Vessell, R. K.; Burkett, P. J. Porosities, Permeabilities, and Microfabrics of Devonian Shales. In *Microstructure of Fine-Grained Sediments*; Springer, 1991; pp 109−119.

(30) Luffel, D. L.; Guidry, F. K. New Core Analysis Methods for Measuring Reservoir Rock Properties of Devonian Shale. *J. Pet. Technol.* **1992**, *44*, 1184−1190.

(31) Bustin, R. M.; Bustin, A. M. M.; Columbia, B.; Cui, X.; Ross, D. J. K. In *Impact of Shale Properties on Pore Structure and Storage Characteristics*, SPE Shale Gas Production Conference, 2008.

(32) Franquet, M.; Ibrahim, M.; Wattenbarger, R. A.; Maggard, J. B. In *Effect of Pressure-Dependent Permeability in Tight Gas Reservoirs, Transient Radial Flow*, Canadian International Petroleum Conference, 2004; pp 1−10.

(33) Mckernan, R.; Mecklenburgh, J.; Rutter, E.; Taylor, K. Microstructural Controls on the Pressure-Dependent Permeability of Whitby Mudstone. *Geol. Soc.* **2017**, *454*, 39−66.

(34) Vairogs, J.; Heam, C. L.; Dareing, D. W.; Rhoades, V. W. Effect of Rock Stress on Gas Production. *J. Pet. Technol.* **1971**, *5*, 1161−1167.

(35) Vairogs, J.; Rhoades, V. W. Pressure Transient Tests in Formations Having Stress-Sensitive Permeability. *J. Pet. Technol.* **1973**, *25*, 965−970.

(36) Ostensen, R. W. The Effect of Stress-Dependent Permeability on Gas Production and Well Testing. *SPE Form. Eval.* **1986**, 227−235.

(37) Soeder, D. J.; Sharma, S.; Pekney, N.; Hopkinson, L.; Dilmore, R.; Kutchko, B.; Stewart, B.; Carter, K.; Hakala, A.; Capo, R. An Approach for Assessing Engineering Risk From Shale Gas Wells in the United States. *Int. J. Coal Geol.* **2014**, *126*, 4−19.

(38) Pedrosa, O. In *Pressure Transient Response in Stress-Sensitive Formations*, SPE California Regional Meeting; 1986; p 15115.

(39) Klkanl; Pedrosa. Perturbation analysis of stress-sensitive reservoirs. *SPE Form. Eval.* **1992**, *29*, No. A160.

(40) Samaniego, V. F.; Cinco, L. H. Production Rate Decline in Pressure-Sensitive Reservoirs. *J. Can. Pet. Technol.* **1980**, *19*, 75−86.

(41) Raghavan, R.; Chin, L. Y.; Company, P. P. In *Productivity Changes in Reservoirs With Stress-Dependent Permeability*, SPE Annual Technical Conference and Exhibition, Society of Petroleum Engineers, 2002.

(42) Freeman, C. M. In *A Numerical Study of Microscale Flow Behavior in Tight Gas and Shale Gas Reservoir Systems*, SPE Annual Technical Conference and Exhibition, Society of Petroleum Engineers, 2010; pp 19−22.

(43) Wang, J.; Luo, H.; Liu, H.; Cao, F.; Li, Z.; Sepehrnoori, K. An Integrative Model to Simulate Gas Transport and Production Coupled with Gas Adsorption, Non-Darcy Flow, Surface Diffusion, and Stress Dependence in Organic-Shale Reservoirs. *SPE J.* **2017**, *22*, 244−264.

(44) Tian, F.; Wang, X.; Xu, W. A Semi-Analytical Model for Multiple-Fractured Horizontal Wells in Heterogeneous Gas Reservoirs. *J. Pet. Sci. Eng.* **2019**, *183*, No. 106369.

(45) Wei, M.; Duan, Y.; Dong, M.; Fang, Q. Blasingame Decline Type Curves with Material Balance Pseudo-Time Modified for Multi-Fractured Horizontal Wells in Shale Gas Reservoirs. *J. Nat. Gas Sci. Eng.* **2016**, *31*, 340−350.

(46) Zhang, R.; Zhang, L.; Wang, R.; Zhao, Y.; Huang, R. Simulation of a Multistage Fractured Horizontal Well with Finite Conductivity in Composite Shale Gas Reservoir through Finite- Element Method. *Energy Fuels* **2016**, *30*, 9036−9049.

(47) Wang, T.; Tian, S.; Zhang, W.; Ren, W.; Li, G. Production Model of a Fractured Horizontal Well in Shale Gas Reservoirs. *Energy Fuels* **2021**, *35*, 493−500.

(48) Lane, H. S.; Watson, A. T.; Lancaster, D. E. In *Identifying and Estimating Desorption From Devonian Shale Gas Production Data*, SPE Annual Technical Conference and Exhibition, Society of Petroleum Engineers, 1989.

(49) Ozkan, E.; Raghavan, R.; Petroleum, P.; Retd, C.; Apaydin, O. G. In *Modeling of Fluid Transfer from Shale Matrix to Fracture Network*, SPE Annual Technical Conference and Exhibition, Society of Petroleum Engineers, 2010; p 18.

(50) Zhao, Y. L.; Zhang, L. H.; Luo, J. X.; Zhang, B. N. Performance of Fractured Horizontal Well with Stimulated Reservoir Volume in Unconventional Gas Reservoir. *J. Hydrol.* **2014**, *512*, 447−456.

(51) Wang, H. T. Performance of Multiple Fractured Horizontal Wells in Shale Gas Reservoirs with Consideration of Multiple Mechanisms. *J. Hydrol.* **2014**, *510*, 299−312.

(52) Su, Y.; Zhang, Q.; Wang, W.; Sheng, G. Performance Analysis of a Composite Dual-Porosity Model in Multi-Scale Fractured Shale Reservoir. *J. Nat. Gas Sci. Eng.* **2015**, *26*, 1107−1118.

(53) Lu, T.; Liu, S.; Li, Z. A New Approach to Model Shale Gas Production Behavior by Considering Coupled Multiple Flow Mechanisms for Multiple Fractured Horizontal Well. *Fuel* **2019**, *237*, 283−297.

(54) Tian, F.; Wang, X.; Xu, W. Journal of Petroleum Science and Engineering A Semi-Analytical Model for Multiple-Fractured Horizontal Wells in Heterogeneous Gas Reservoirs. *J. Pet. Sci. Eng.* **2019**, *183*, No. 106369.

(55) Jiang, L.; Liu, J.; Liu, T.; Yang, D. Semi-Analytical Modeling of Transient Rate Behaviour of a Horizontal Well with Multistage Fractures in Tight Formations Considering Stress-Sensitive Effect. *J. Nat. Gas Sci. Eng.* **2020**, *82*, No. 103461.

(56) Li, T.; Tan, Y.; Dai, S.; Zhou, X.; Yu, J.; Yang, Q. Semi-Analytical Model Based on the Volumetric Source Method to Production Simulation from Nonplanar Fracture Geometry in Tight Oil Reservoirs. *ACS Omega* **2021**, *6*, 615−622.

(57) Lu, T.; Li, Z.; Lai, F.; Meng, Y.; Ma, W.; Sun, Y. Blasingame Decline Analysis for Variable Rate/Variable Pressure Drop: A Multiple Fractured Horizontal Well Case in Shale Gas Reservoirs. *J. Pet. Sci. Eng.* **2019**, *178*, 193−204.

(58) Langmuir, I. The Constitution and Fundamental Properties of Solids and Liquids. *J. Franklin Inst.* **1917**, *183*, 102−105.

(59) Zhao, W.; Wang, K.; Liu, S.; Ju, Y.; Zhou, H.; Fan, L.; Yang, Y.; Cheng, Y.; Zhang, X. Asynchronous Difference in Dynamic Characteristics of Adsorption Swelling and Mechanical Compression of Coal: Modeling and Experiments. *Int. J. Rock Mech. Min. Sci.* **2020**, *135*, No. 104498.

(60) Crank, J. *The Mathematics of Diffusion*; Oxford University Press, 1956.

(61) Darabi, H.; Ettehad, A.; Javadpour, F.; Sepehrnoori, K. Gas Flow in Ultra-Tight Shale Strata. *J. Fluid Mech.* **2012**, *710*, 641−658.

(62) Ancell, K. L.; Lambert, S. T.; Johnson, F. S. In *Analysis of the Coalbed Degasification Process at a Seventeen Well Pattern in the Warrior Basin of Alabama*, SPE Unconventional Gas Recovery Symposium, Society of Petroleum Engineers, 1980; p 88971.

(63) Celis, V.; Silva, R.; Ramones, M.; Guerra, J.; Da Prat, G. A New Model for Pressure Transient Analysis in Stress Sensitive Naturally Fractured Reservoirs. *SPE Adv. Technol. Ser.* **1994**, *2*, 126−135.

(64) Gutierrez, M.; Nyga, R. Stress-Dependent Permeability of a de-Mineralised Fracture in Shale. *Mar. Pet. Geol.* **2000**, *17*, 895−907.

(65) An, C.; Killough, J.; Mi, L. Journal of Petroleum Science and Engineering Stress-Dependent Permeability of Organic-Rich Shale Reservoirs: Impacts of Stress Changes and Matrix Shrinkage. *J. Pet. Sci. Eng.* **2019**, *172*, 1034−1047.

(66) Kikani, J.; Pedrosa, O. A., Jr Perturbation Analysis of Stress-Sensitive Reservoirs. *SPE Form. Eval.* **1991**, *6*, 379−386.

(67) Yeung, K.; Chakrabarty, C.; Zhang, X. An Approximate Analytical Study of Aquifers with Pressure-Sensitive Formation Permeability. *Water Resour. Res.* **1993**, *29*, 3495−3501.

(68) Van Everdingen, A. F.; Hurst, W. The Application of the Laplace Transformation to Flow Problems in Reservoirs. *J. Pet. Technol.* **1949**, *1*, 305−324.

(69) Ren, J.; Guo, P. A General Analytical Method for Transient Fl Ow Rate with the Stress-Sensitive Effect. *J. Hydrol.* **2018**, *565*, 262−275.